Co/Co_2P Nanoparticles Encapsulated within Hierarchically Porous Nitrogen, Phosphorus, Sulfur Co-doped Carbon as Bifunctional Electrocatalysts for Rechargeable Zinc-Air Batteries

Likai Wang,*[a] Yinggang Sun,[a] Shenzhi Zhang,[a] Hexiang Di,[a] Qiming Liu,[b] Xin Du,*[c] Zhongfang Li,[a] Kai Yang,[a] and Shaowei Chen*[b]

Developing high performance nonprecious metal-based electrocatalysts has become a critical first step towards commercial applications of metal-air batteries. Herein, nanocomposites based on Co/Co_2P nanoparticles encapsulated within hierarchically porous N, P, S co-doped carbon are prepared by controlled pyrolysis of zeolitic imidazolate frameworks (ZIF-67) and poly (cyclotriphosphazene-co-4,4′-sulfonyldiphenol) (PZS). The resulting Co/Co_2P@NPSC nanocomposites exhibit apparent oxygen reduction reaction (ORR) and evolution reaction (OER) catalytic performance, and are used as the reversible oxygen catalyst for zinc-air batteries (ZABs). Density functional theory (DFT) calculations exhibit that Co_2P could provide active sites for the ORR and promote the conversion between the adsorbed intermediates, and porous N,P,S co-doped carbon with Co_2P nanoparticles also improves the exposure of actives sites and endows charge transport. Liquid-state ZABs with Co/Co_2P@NPSC as the cathode catalysts demonstrate the greater power density of 198.1 $mW\,cm^{-2}$ and a long cycling life of 50 h at 10 $mA\,cm^{-2}$, likely due to the encapsulation of Co/Co_2P nanoparticles by the carbon shell. Solid-state ZABs also display a remarkable performance with a high peak power density of 74.3 $mW\,cm^{-2}$. Therefore, this study indicates the meaning of the design and engineering of hierarchical porous carbon nanomaterial as electrocatalyst for rechargeable metal-air batteries.

Introduction

Rechargeable metal-air batteries have been attracting much attention as a new effective electrochemical energy technology, owing to their high theoretical energy density, lower costs, and environment-friendly.[1,2] Of these, rechargeable ZABs with nonflammable and high ionic conductivity water electrolytes are of particular interest, thanks to their safe operation and high rate output.[3–7] Yet, the sluggish electron-transfer kinetics at the air cathode, which entails ORR during discharge and OER during charge, has been found to severely hinder the energy conversion rate and rechargeability of ZAB.[8–10] Precious metal-based nanoparticles (e.g., Pt, Pd, Ir and Ru) have been used widely as the electrocatalysts towards ORR and OER.[11–13] However, their high costs, low natural abundance, and limited stability have rendered it challenging to achieve large-scale commercialization of the technology. Additionally, these catalysts are generally active to either ORR or OER. Therefore, it is imperative to design robust, high-efficiency bifunctional electrocatalysts for metal-air batteries.

Now Considerable efforts have been dedicated to engineer nonprecious metal-based electrocatalysts, such as, transition-metal oxides, metal-carbon nanocomposites, as well as heteroatom-doped carbon.[10,14–17] Among these, transition-metal oxides are known to show high electrocatalytic activity and good durability in metal-air batteries, but the performance is compromised by the poor electrical conductivity.[18] By contrast, porous carbon, with a high pore volume and surface area, can promote mass transport of reaction species and have emerged as a viable alternative as low-cost, high-efficiency catalysts for metal-air batteries.[19] Meanwhile, metal-carbon nanocomposites (e.g., Fe, Co, and Ni) have attracted great attention, where their high electrocatalytic activity can be gained by the dopant of heteroatom into the carbon matrix and formation of metal hybrid nanoparticles.[18,20, 21] Of these, transition-metal phosphides (TMPs) have been known as hopeful oxygen electrocatalysts, as electronegative P can act as a Lewis acid and grab the electrons from metal centers to manipulate the charge distribution within the materials.[3,22–25] For instance, cobalt phosphide has demonstrated excellent electrocatalytic activity towards HER (hydrogen evolution reaction) and OER.[26–29] However, the electron transport kinetics of Co_2P is sluggish due to the strong binding force of surface Co atom with the

[a] Dr. L. Wang, Y. Sun, S. Zhang, H. Di, Z. Li, K. Yang
School of Chemistry and Chemical Engineering
Shandong University of Technology
Zibo, Shandong 255049, P. R. China
E-mail: lkwangchem@sdut.edu.cn
[b] Q. Liu, S. Chen
Department of Chemistry and Biochemistry
University of California
1156 High Street, Santa Cruz, California 95064, United States
E-mail: shaowei@ucsc.edu
[c] X. Du
School of Chemistry
Zhengzhou University
Zhengzhou, Henan 450001, P. R. China
E-mail: dux@zzu.edu.cn

Supporting information for this article is available on the WWW under https://doi.org/10.1002/celc.202101246

adsorbed intermediates, so their electrocatalytic activity towards ORR is limited.[30,31] Then it is a great challenge to fine design and rationally synthesize a robust, durable and high-efficiency bi-functional Co_2P-based catalyst for metal-air batteries.[32] Significantly, the electrocatalytic activity of TMPs can be enhanced by hybridizing TMPs with porous carbon materials, due to synergistic interactions between TMPs and the carbon scaffold,[19,33–36] and electronic modulation by the heteroatom doping (e.g., N, P, S, B, etc.) of the carbon matrix.[25,28,37,38] Therefore, it is very significant to design a synergistic nanocomposite combination between Co_2P materials and heteroatom-doped carbon substrates for satisfying high efficiency oxygen electrodes for metal-air batteries.

In this work, we developed an exquisite hybrid composite based on Co/Co_2P nanoparticles encapsulated within N,P,S co-doped porous carbon by controlled pyrolysis of a cobalt-containing ZIF-67 and PZS. Electrochemical measurements showed enhanced ORR activity and long-term durability compared with commercial Pt/C, whereas the OER activity and stability was comparable to that of RuO_2. With the Co/Co_2P@NPSC composite as the oxygen catalysts, a rechargeable ZAB in liquid electrolyte was fabricated, which demonstrated a high peak power density of 198.1 mW cm^{-2}, a specific capacity of 890.5 mAh g_{Zn}^{-1}, low discharge and charge of polarization, and a long cycling life of 50 h at 10 mA cm^{-2}. Similarly remarkable performance was observed with a solid-state ZAB, which exhibited a high peak power density of 74.3 mW cm^{-2} and a stable cycling life (over 50 cycles at 10 mA cm^{-2}).

Results and Discussion

As illustrated in Figure 1, Co/Co_2P@NPSC was schematically prepared, where involved two major steps. First, ZIF-67 was produced by the mixing of 2-methylimidazole and $Co(NO_3)_2 \cdot 6H_2O$, which displayed a polyhedral shape with the nanoparticles ranging from 150 to 250 nm in diameter, as revealed in SEM measurements (Figure 2a).[39] ZIF-67 was then coated with a calculated amount of PZS and pyrolyzed under 800 °C for 2 h, and followed by dilute sulfuric acid leaching to produce NPSC (Figure 2b).

From Figure 2c, one can see that the Co/Co_2P@NPSC nanocomposites exhibited a hollow-sphere structure of 250–300 nm in diameter. The corresponding XRD patterns were shown in Figure 2d. For Co-NC that was derived pyrolytically from ZIF-67 alone, three major diffraction peaks can be identified at $2\theta =$ 44.2°, 51.5° and 75.9°, which are readily attributed to the characteristic (111), (200) and (220) reflections of metallic cobalt (JCPDS No. 15-0806), suggesting the formation Co nanoparticles in the sample. With the coating of PZS onto ZIF-67 prior to pyrolysis, Co/Co_2P@NPSC-1 (Table S1) exhibited almost identical XRD patterns to those of Co-NC. Yet at increasing PZS to ZIF feed ratio, additional diffraction peaks emerged. For instance, Co/Co_2P@NPSC-2 exhibited a peak at $2\theta = 40.9°$, which was assigned to the (121) facet of Co_2P (JCPDS No. 32-0306), suggestive of the formation of Co_2P.[35] This peak became intensified with Co/Co_2P@NPSC-3 and Co/Co_2P@NPSC-4, whereas for Co/Co_2P@NPSC-5, more peaks appeared at $2\theta = 31.5°$, 36.3°, 48.1°, and 56.7°, due to the (011), (111), (211), and (301) reflections of CoP (JCPDS No. 29-0497), respectively.[40]

In SEM measurements (Figure S1), Co-NC can be seen to display a rough, solid morphology, whereas the Co/Co_2P@NPSC samples all possessed a porous, hollow structure. Then BET was used to evaluate the porosity of the Co/Co_2P@NPSC samples. As depicted in Figure 2e, all Co/Co_2P@NPSC samples exhibited a type IV isotherm, implying the formation of micro- and mesoporous structure; yet the BET specific surface area varied. For instance, the BET specific surface area was about 399.1 m^2 g^{-1} for the Co-NC sample, with the pore size mainly between 3 and 5 nm (Figure 2f), and decreased to 275.6 m^2 g^{-1}

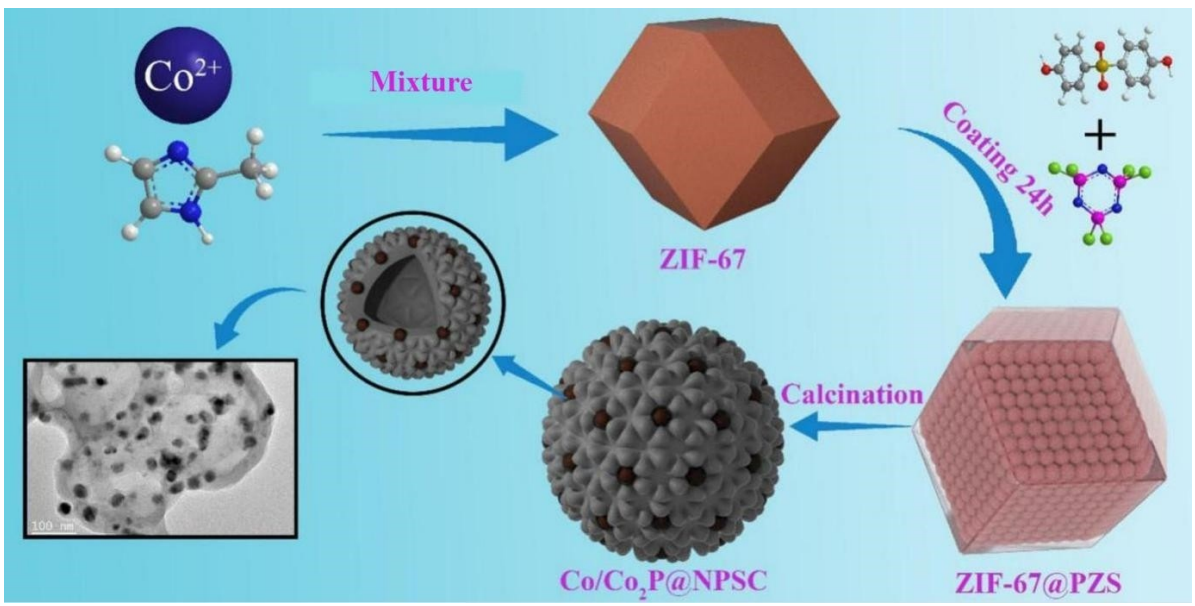

Figure 1. Schematic diagram of the preparation of Co/Co_2P@NPSC nanocomposites.

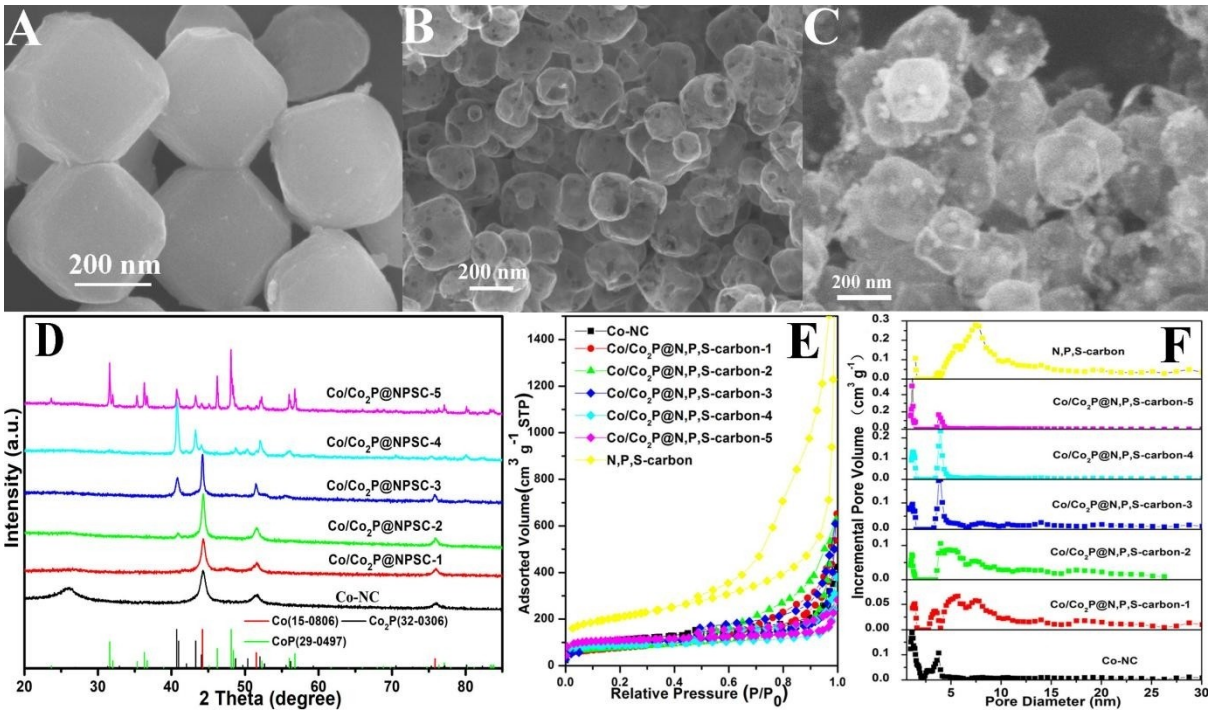

Figure 2. SEM images of ZIF-67 (a), NPSC (b), and Co/Co_2P@NPSC-3 (c). XRD patterns (d), N_2 adsorption/desorption isotherms of Co/Co_2P@NPSC nanocomposites (e) and BJH pore-size distributions of the series of samples (f).

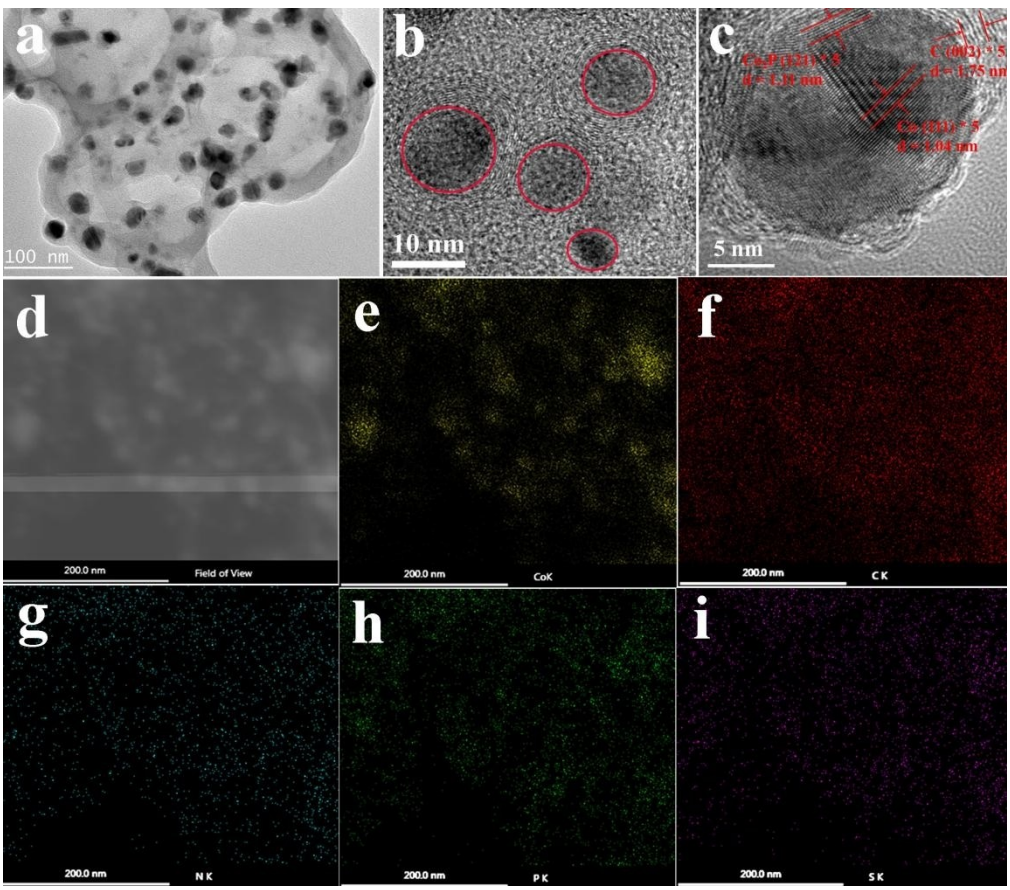

Figure 3. Typical TEM images of Co/Co_2P@NPSC-3 (a–c). Representative HAADF-STEM of Co/Co_2P@NPSC-3 (d), and the elemental mapping of Co (e), C (f), N (g), P (h) and S (i).

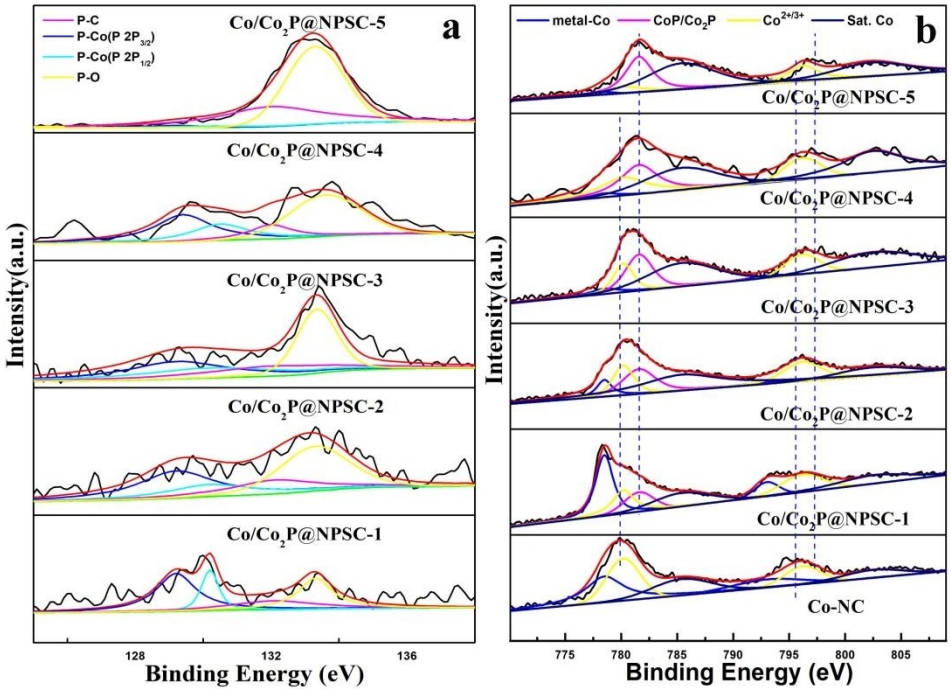

Figure 4. Deconvoluted P 2p (a) and Co 2p (b) XPS spectra of the series of samples.

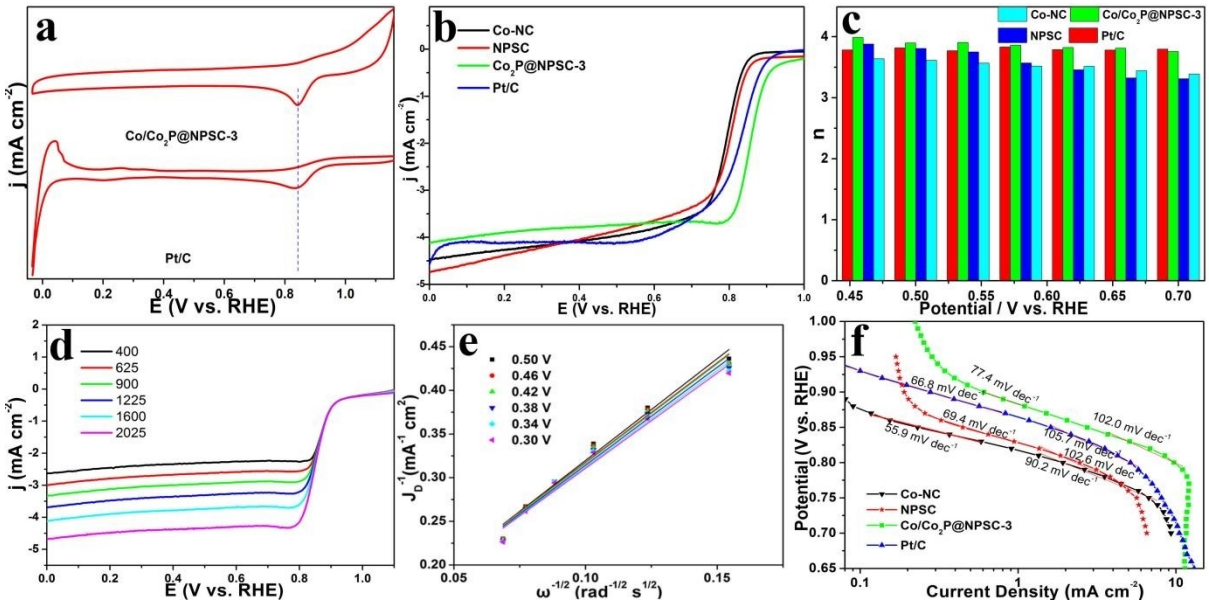

Figure 5. ORR performance of the series of Co/Co_2P@NPSC samples in O_2-saturated 0.1 M KOH. a) CV of Co/Co_2P@NPSC-3 and Pt/C catalyst. b) LSV curves of Co-NC, NPSC, Co/Co_2P@NPSC-3 and Pt/C catalysts at 1600 rpm. c) n of Co-NC, NPSC, Co/Co_2P@NPSC-3 and Pt/C catalysts calculated from the K–L plots. d) LSV curves of Co/Co_2P@NPSC-3 from 400 to 2025 rpm, and e) the K–L plots of Co/Co_2P@NPSC-3. (f) Tafel plots of Co-NC, NPSC, Co/Co_2P@NPSC-3 and Pt/C catalysts.

for Co/Co_2P@NPSC-1, likely due to the formation of the NPSC shell that blocked some of the surface pores. Yet for Co/Co_2P@NPSC-2, it increased slightly to 281.7 $m^2 g^{-1}$, due to the existence of a hollow structure. With a further increasing feed of PZS, the hollow interior expanded accordingly, and the surface area increased to 337.2 $m^2 g^{-1}$ for Co/Co_2P@NPSC-3, 347.7 $m^2 g^{-1}$ for Co/Co_2P@NPSC-4 and 420.1 $m^2 g^{-1}$ Co/Co_2P@NPSC-5. Note that the porous structure (Figure 2f) is conducive to mass transfer of electrocatalytic reactions.[41–43]

Consistent results were also confirmed in HRTEM images. As illustrated in Figure 3(a, b), the Co/Co_2P@NPSC-3 sample exhibited a number of nanoparticles encapsulated in a carbon shell; and the thickness of carbon shell increased with the increasing feed of PZS. In fact, from Figure S2, the NPSC

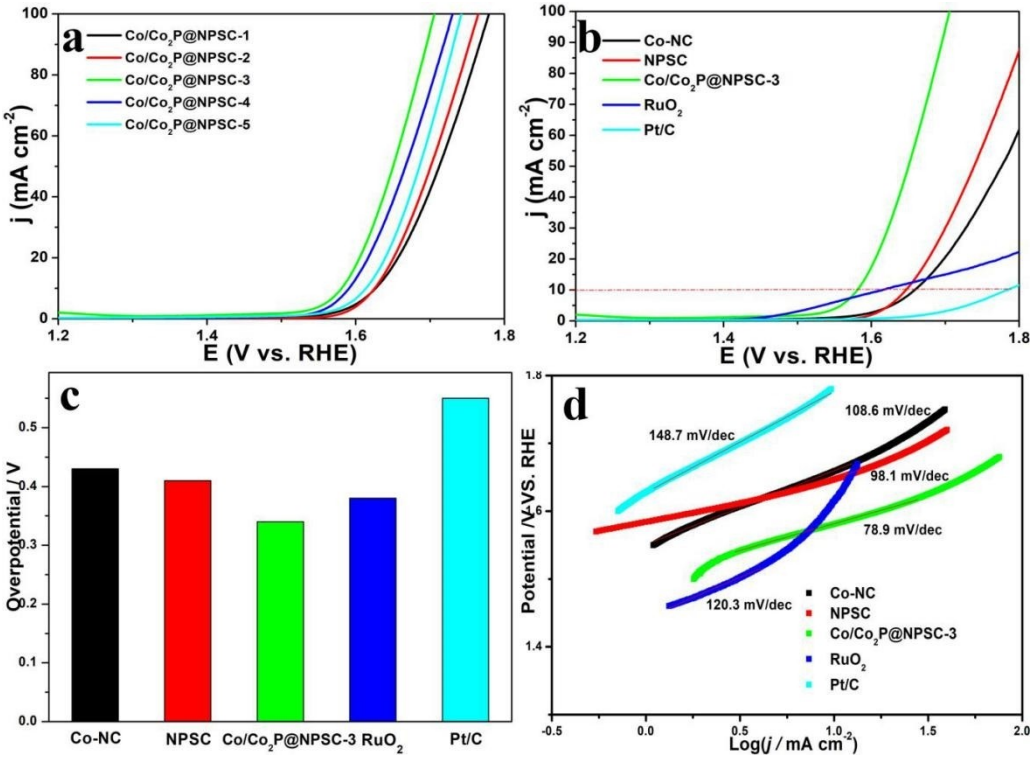

Figure 6. OER performances of as-prepared catalysts in 1 M KOH. a) OER curves of the series of the Co/Co_2P@NPSC-3 catalysts. b) OER polarization curves of Co-NC, N,P,S-Carbon, Co/Co_2P@N,P,S-carbon-3, Pt/C and RuO_2 catalysts with the speed of 1600 rpm. c) Comparison of $\eta_{10,OER}$ among the different catalysts, and d) the corresponding Tafel plots.

thickness was estimated to be 1.4 ~ 2.7 nm for Co/Co_2P@NPSC-1, 5 ~ 6 nm for Co/Co_2P@NPSC-2, 9.0 ~ 11.2 nm for Co/Co_2P@NPSC-3, *ca.* 21.3 nm for Co/Co_2P@NPSC-4, and *ca.* 32.4 nm for Co/Co_2P@NPSC-5 (Table S1). In addition, the nanoparticles displayed well-defined lattice fringes (Figure 3c), which included three interplanar distances, 0.350, 0.222, and 0.201 nm, corresponding to the carbon (002), Co_2P (121) and Co (111) planes, respectively, in consistent with results from the XRD patterns (Figure 2d).[28] Furthermore, the elemental mapping analysis based on HAADF-STEM measurements (Figure 3d–i) demonstrated that the C, N, P and S elements were well distributed on the Co/Co_2P@NPSC-3 sample, whereas Co was concentrated at the nanoparticles.

The valence state and elemental composition of the series of samples were then investigated by XPS spectra. As depicted in Figure S3, the Co, C, N, P and S elements can be clearly discerned for the samples, and their contents were displayed in Table S2. The deconvoluted scans of the C 1s electrons are displayed in Figure S4a, where three major components can be resolved at 284.8, 285.8, 287.6 and 289.1 eV, due to C–C, C–N/C–S/C–P, C=O/C=N and O–C=O, respectively. Note that the constituent of C–N/C–S/C–P suggests successful doping of N and S into the porous carbon matrix.[44,45] Figure S4b shows the deconvoluted N 1s spectra of the samples, and deconvolution yields four peaks at 398.6 eV, 399.6 eV, 400.9 eV, and 403.5 eV, which should be ascribed to pyridinic N, pyrrolic N, graphitic N and oxidized N, respectively.[5,46] The contents of these N species in the series of samples are summarized in Table S3, where Co/Co_2P@NPSC-3 exhibited the highest content of pyridinic N (3.23 at%).[19] In Figure 4a, a doublet can be found at 129.2 eV for P–Co ($P\,2p_{3/2}$) and 130.2 eV for P–Co ($P\,2p_{1/2}$) in the high-resolution P 2p spectra, due to P in CoP/Co_2P; whereas the peak at 132.3 eV indicates the formation of P–C bond, and that at 133.3 eV due to the P–O bond, suggesting the doping of P into the C shell.[47] Figure 4b shows the high-resolution Co 2p spectra, where the Co-NC sample exhibited two doublets at 778.5/793.0 eV and 780.2/796.2 eV, due to the $2p_{3/2}$ and $2p_{1/2}$ electrons of metallic Co and $Co^{2+/3+}$ (the latter most likely arose from surface oxidation), respectively.[19,48] For the Co/Co_2P@NPSC samples, in addition to the $Co^{2+/3+}$ doublet at 780.2/796.2 eV, another peak can be resolved at 781.6 eV, consistent with the formation of Co_2P and CoP nanoparticles (Table S3).[35] In addition, the binding energy of $Co\,2p_{3/2}$ (778.5 eV) can be seen to show a positive shift, whereas that of $P\,2p_{3/2}$ (129.2 eV) demonstrates a negative-shift, in comparison to those of metallic Cobalt (about 778.1–778.2 eV) and P (130.2 eV), indicating the transfer of electrons from Co to P.[31,49] The S 2p spectra (Figure S4c) can be deconvoluted into three peaks at 163.8, 165.2 and 168.5 eV, due to the $2p_{3/2}$ and $2p_{1/2}$ electrons of C–S-C and the oxidized S, respectively.[39] These results are consistent with those from the above XRD, BET and HR-TEM measurements, confirming the doping of heteroatoms (N, P and S) into the carbon matrix and incorporation of Co species in the samples, which facilitate the catalytic activity toward both OER and ORR (*vide infra*).[49]

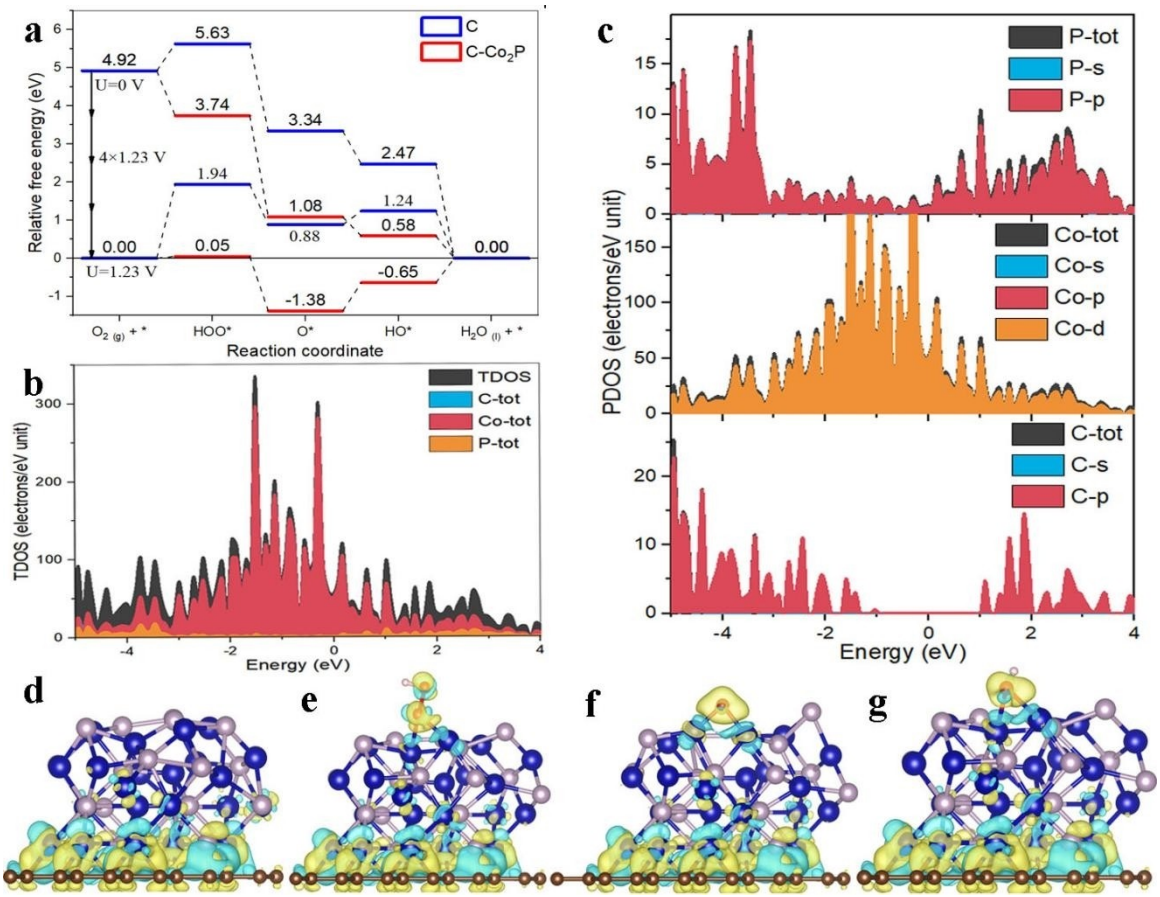

Figure 7. a) Free energy diagram of ORR on C and C–Co_2P cluster model; b, c) DOS of C–Co_2P cluster. Calculated charge density differences for C–Co_2P cluster (d), adsorbates OOH* (e), O* (f), and (g) OH* on the model.

Notably, the series of Co/Co_2P@NPSC nanocomposites demonstrated high electrocatalytic activity towards ORR in alkaline solution. From the LSV tests in at 1600 rpm, it could be observed that the electrocatalytic performance varied apparently among the series of Co/Co_2P@NPSC samples. As illustrated in Figure S5, the onset potential (E_{onset}) and half-wave potential ($E_{1/2}$) could be estimated to be +0.93 and +0.80 V for Co/Co_2P@NPSC-1, +0.95 V and +0.82 V for Co/Co_2P@NPSC-2, +0.99 V and +0.84 V for Co/Co_2P@NPSC-3, +0.89 V and +0.79 V for Co/Co_2P@NPSC-4, and +0.88 V and +0.78 V for Co/Co_2P@NPSC-5. In other words, the Co/Co_2P@NPSC-3 sample performed as the best ORR electrocatalyst among the series, likely due to the combined contributions of both the Co and Co_2P nanoparticles and doped carbon scaffold.

The ORR performance of Co/Co_2P@NPSC-3 was further investigated by CV measurements in both nitrogen and oxygen-saturated 0.1 M KOH aqueous solution, at the side of Pt/C. As depicted in Figure 5a, while there was no apparent cathodic peak in the voltammetric profiles in the N_2-saturated solution, a clearly reduction peak appeared at +0.85 V in O_2-saturated solution, suggesting effective reduction of oxygen; and the peak potential was more positive than that of Pt/C (+0.84 V), implying a better catalytic performance of Co/Co_2P@NPSC-3. To further explore the ORR performance, LSV curves were collected in 0.1 M KOH (O_2-saturated) solution at 10 mV s^{-1}, and the results are consistent with the CV data (Figure 5b). Co/Co_2P@NPSC-3 demonstrates E_{onset} of +1.00 V and $E_{1/2}$ of +0.86 V, markedly higher than those of Co-NC (+0.85 and +0.77 V), NPSC (+0.87 and +0.78 V) and Pt/C catalysts (+0.98 and +0.83 V), further confirming that Co/Co_2P@NPSC possessed the best electrocatalytic activity for ORR within the present experimental context.

The ORR kinetics was then evaluated by Koutecky-Levich (K–L) analysis, [Eqs. (1–3)]:

$$\frac{1}{J} = \frac{1}{J_k} + \frac{1}{J_L} = \frac{1}{B\omega^{1/2}} + \frac{1}{J_k} \quad (1)$$

$$B = 0.62\, nFC_0 D_0^{2/3} \nu^{-1/6} \quad (2)$$

$$J_k = nFkC_0 \quad (3)$$

where J represents the experimental current density, the kinetic and diffusion-limited current density are denoted as J_K and J_L, respectively, stands for the rotation rate, n is on behalf of the number of electron transfer, F is Faradaic constant (96485 C mol^{-1}), C_0 is the dissolved O_2 bulk concentration, D_0 is the coefficient of diffusion of O_2 in 0.1 M KOH solution, ν is the

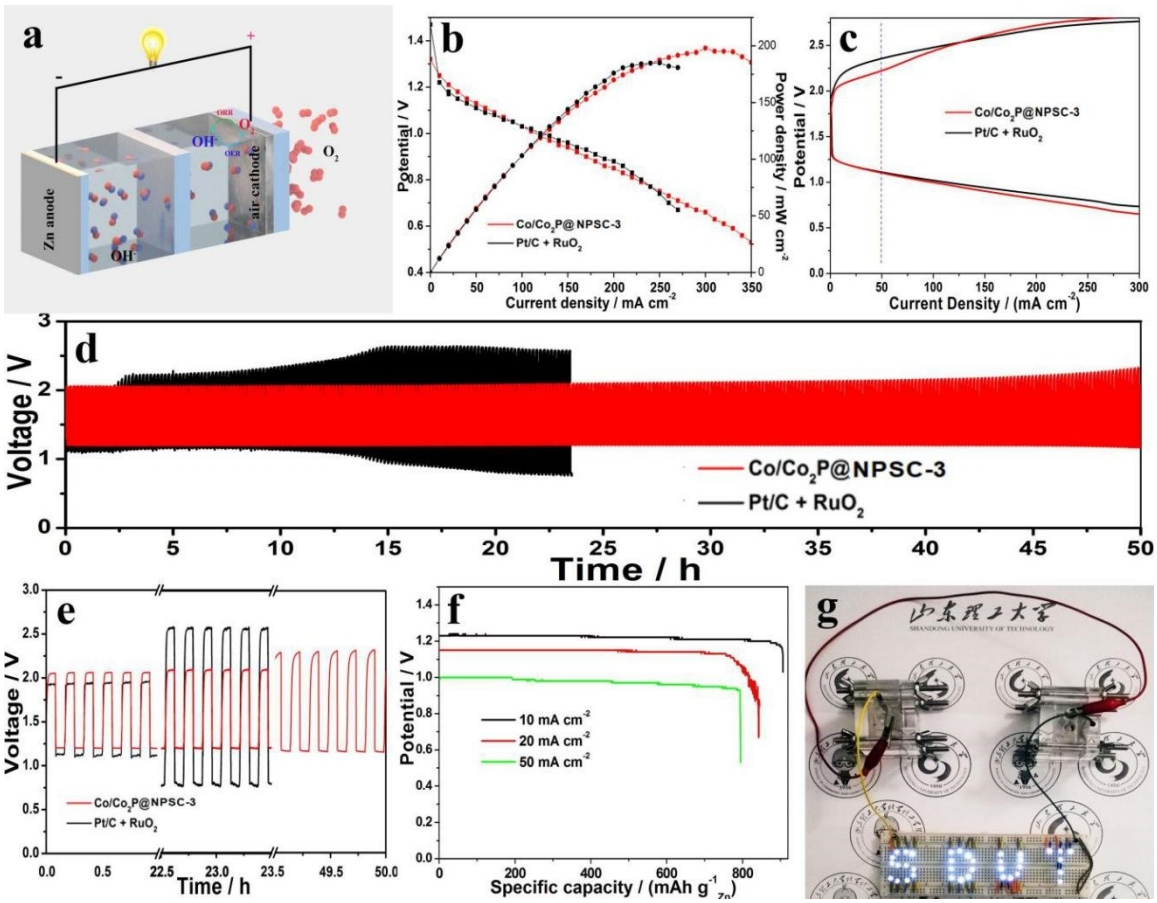

Figure 8. a) Sketch illustration of a rechargeable ZAB. b) Discharge and power density curves of ZAB using Co/Co_2P@NPSC-3, or a Pt/C + RuO_2 mixture as the oxygen electrocatalyst. c) Voltage and current density curves of ZAB using Co/Co_2P@NPSC-3, or a Pt/C + RuO_2. d, e) charge and discharge data of ZAB at 10 mA cm^{-2} in a short period (10 min). f) Long time discharge curves of ZAB with Co/Co_2P@NPSC-3 as the cathode catalysts at different current density. g) A white LED lit by two liquid ZABs in series with Co/Co_2P@NPSC-3 as air-cathode.

kinetic viscosity of KOH solution, and k is the constant of electron transfer rate. From Figure 5c, n was calculated to be about 3.85–4.00 for Co/Co_2P@NPSC-3 in the potential range of 0.45–0.70 V, which is higher than those of Co-NC (3.4–3.7) and NPSC (3.35–3.93), and similar to that of Pt/C (3.90–3.95), implying that ORR on Co/Co_2P@NPSC proceeded via the 4-electron pathway. Meanwhile, the K–L plots (Figure 5d and e) of Co/Co_2P@NPSC-3 can be seen to exhibit good linearity with a same slope at different potentials, confirming that the ORR process conformed to the first-order reaction of kinetics with reference to the dissolved O_2 concentration.[50,51] Consistent behaviors were shown for other samples, as manifested in Figure S6 and S7.

The Tafel plots are demonstrated in Figure 5f, where the Tafel slope was found to be 55.9 mV dec^{-1} for Co-NC, 69.4 mV dec^{-1} for NPSC, 77.4 mV dec^{-1} for Co/Co_2P@NPSC-3, and 66.8 mV dec^{-1} for Pt/C in the low-overpotential regime, indicating that the reaction kinetics for ORR was largely determined by a pseudo 2-electron reaction. In the high overpotential region, the Tafel slope was 90.2 mV dec^{-1} for Co-NC, 102.6 mV dec^{-1} for NPSC, 102.0 mV dec^{-1} for Co/Co_2P@NPSC-3, and 105.7 mV dec^{-1} for Pt/C ($< +0.85$ V), suggesting that the first electron transfer to O_2 might be the ORR rate-determining step.[52,53]

The samples also exhibited efficient catalytic activity towards OER. Among the series of samples, Co/Co_2P@NPSC-3 demonstrates the smallest overpotential, again standing out as the best sample (Figure 6a). From Figure 6b and c, the Co/Co_2P@NPSC-3 sample can be seen to display a higher specific current and much lower onset potential than those of Co-NC, NPSC, RuO_2 and Pt/C. Specifically, Co/Co_2P@NPSC-3 exhibited an overpotential ($\eta_{10,OER}$) of about 325 mV at the current density of 10 mA cm^{-2}, which was lower than those of Co-NC (429 mV), NPSC (418 mV), RuO_2 (387 mV) and Pt/C (545 mV), indicating that Co/Co_2P@NPSC-3 possessed the best electrocatalytic activity for OER. Meanwhile, the Tafel plots were depicted in Figure 6d, and the Tafel slope was estimated to be 78.9 mV dec^{-1} for Co/Co_2P@NPSC-3, which was also lower than those of Co-NC (108.6 mV dec^{-1}), NPSC (98.1 mV dec^{-1}), RuO_2 (120.1 mV dec^{-1}), and Pt/C (148.7 mV dec^{-1}), implying the fastest reaction kinetics.[54,55] This is also consistent with the trend of the aforementioned overpotential values.

The high electrocatalytic performance of Co/Co_2P@NPSC-3 may be attributed to the interactions between Co/Co_2P nanoparticles and NPSC. First of all, the high specific surface area of

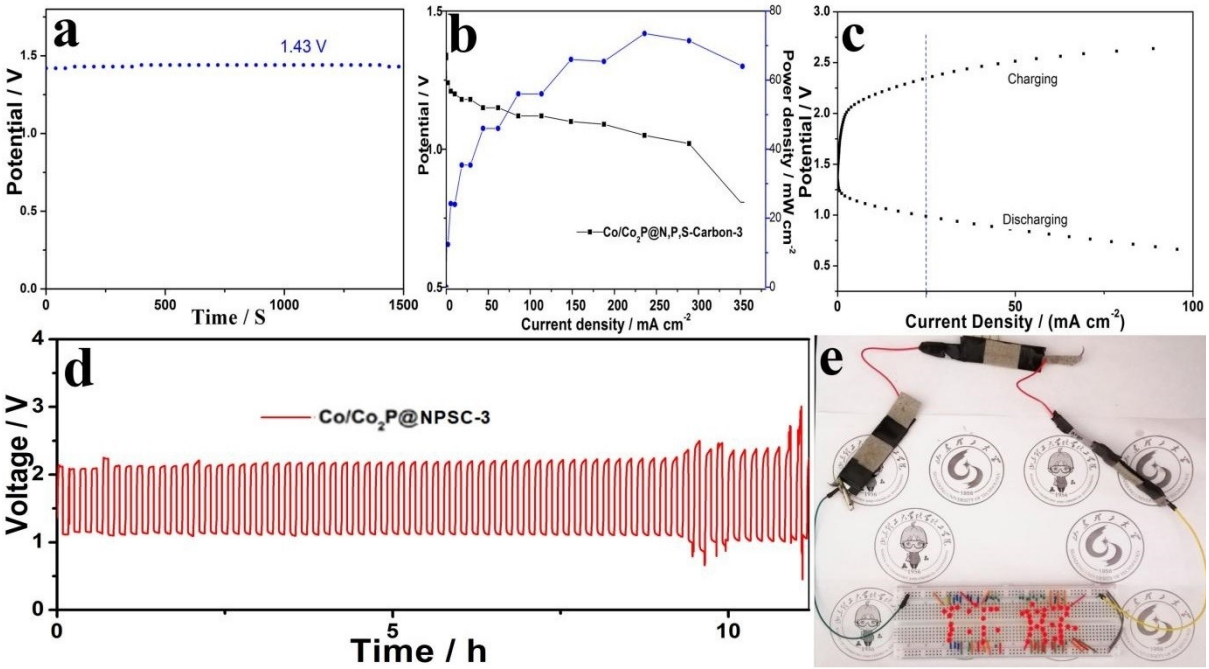

Figure 9. a) OCV of all-solid-state ZAB based on Co/Co_2P@N,P,S-carbon-3 as oxygen catalysts. b) Polarization and power density curves of all-solid-state ZAB using Co/Co_2P@N,P,S-carbon-3 as oxygen catalysts. c) Voltage and current density curves using Co/Co_2P@N,P,S-carbon-3 as oxygen catalysts. d) Discharge-charge cycling profiles at 10 mA cm^{-2} in a short period (10 min). e) Image of a lighted red LED powered by three all-solid-state ZABs interconnected in series.

the NPSC shell allowed ready access to the catalytic active sites and the high porosity facilitated mass transport of important species in the electrocatalytic reactions, such as O_2, H^+, OH^- and H_2O.[56,57] Secondly, the interfacial charge transfer between the metal core and the NPSC carbon shell that handle the electronic interactions between the intermediates and catalysts surface could promote the catalytic activities. The NPSC carbon shell can also prevent the aggregation and the corrosion of metal core, leading to excellent stability.[58] Thirdly, the N, P and S dopants in the porous carbon shell could induce charge redistribution of the carbon scaffold and the formation of the electrocatalytic active sites towards ORR and OER.[25,53,59,60] For instance, N doping can modulate the electron-neutrality of neighboring carbon atoms and improve the adsorption of O_2 species.[61,62] As reported in previous studies,[21,29] DFT calculations showed that the reverse electronegativity between P and S can lead to a unique electron-donor property in S-phosphide and the synergistic coupling effect between P, S and carbon, which facilitates ORR electrocatalysis.[2,3] Last but not least, the presence of metallic cobalt as a conductive electrocatalytic material provided more active sites, and Co_2P played a key role in optimizing the catalytic active site towards ORR, where charge transfer between P and Co led to activation of the encapsulated carbon shell, as observed previously.[19,33]

To further study the ORR activity of Co_2P, DFT calculations were conducted by clusters model. Two models were constructed (Figure S8) including C and C–Co_2P based on the results of XPS and XRD. The optimized configurations with the adsorbates OOH*, O*, and OH* as depicted in Figure S8. Based on the typical ORR reaction pathway of $O_2 \rightarrow {}^*O_2 \rightarrow {}^*OOH \rightarrow {}^*O \rightarrow {}^*OH \rightarrow H_2O$, the free energy diagram at the equilibrium potential ($U_{RHE} = 0$ V) is displayed in Figure a. The Gibbs free energy diagram of the ${}^*O_2 \rightarrow {}^*OOH$ on graphene is uphill process, but all the process of C–Co_2P is downhill process, indicating that Co_2P could significantly promote the ORR. From the calculated density of states (DOS) in Figure b–c and Figure S9, one can see that the highest d orbit density of Co at Fermi level also confirmed that d orbit electrons effectively enhance the activity in ORR reaction. Meanwhile, the charge density difference further confirmed the above results in Figure 7(d–g). Additionally, Co_2P heterojunction model was also conducted to evaluate the electrocatalytic performance of Co_2P as observed in Figure S10, but the heterojunction model is far less reasonable and sufficient than the cluster model. In sum, DFT calculations exhibit that Co_2P could provide active sites for ORR and promote the conversion between the adsorbed intermediates, and N,P,S co-doped carbon with Co_2P nanoparticles also improve the exposure of actives sites and endow charge transport.

Motivated by the remarkable activity of Co/Co_2P@NPSC-3 toward both ORR and OER, it was then used as bifunctional electrocatalysts to construct rechargeable ZABs (Figure 8a). As illustrated in Figure 8b, the ZAB demonstrated a peak power density of 198.1 mW cm^{-2}, much higher than that of a mix commercial Pt/C and RuO_2 catalysts based ZAB (183.8 mW cm^{-2}). Then the corresponding discharge and charge polarization curves of ZABs are shown in Figure 8c, and the ZAB with Co/Co_2P@NPSC-3 demonstrated a smaller voltage gap

(0.97 V) than that with Pt/C + RuO_2 (1.16 V) at 50 mA cm^{-2}, implying a higher charge-discharge capacity.

Additionally, the cycle life of the air-cathode was investigated by the charge-discharge measurements at 10 mA cm^{-2} in a short period (10 min), as displayed in Figure 8d and e. Obviously, the ZAB with Co/Co_2P@NPSC-3 displayed superior cycling stability for more than 300 cycles (or 50 h equivalent), much better than that of Pt/C + RuO_2 (only 141 cycles, or 23.5 h). As illustrated in Figure 8e, the initial voltage gap was 0.85 and 0.83 V for Co/Co_2P@NPSC-3 and Pt/C + RuO_2, respectively. Notably, it increased to 1.80 V after 23.5 h for Pt/C + RuO_2, but remained virtually unchanged at 0.88 V for Co/Co_2P@NPSC-3. The round-trip efficiency of Pt/C + RuO_2 decreased significantly from 57.2% to 30.1% after a 23.5 h charging-discharging cycle test, in contrast to a slight decrease from 58.5% to 57.7% for Co/Co_2P@NPSC-3. In fact, the battery charging-discharging cycles of Co/Co_2P@NPSC-3 remained stable and only decayed to 50.4% at 50 h, further implying the excellent stability of Co/Co_2P@NPSC-3, which actually outperformed a number of catalysts reported previously (Table S4). The long time discharge curves of ZAB with Co/Co_2P@NPSC-3 at different current density of 10, 20 and 50 mA cm^{-2} are displayed in Figure 8f, and the specific capacity normalized to the loss mass of Zn plate was about 890.5 mAh g_{Zn}^{-1} (10 mA cm^{-2}), 770.8 mAh g_{Zn}^{-1} (20 mA cm^{-2}) and 748.6 mAh g_{Zn}^{-1} (50 mA cm^{-2}). To demonstrate the application of such ZABs, a white LED light of the "SDUT" logo can be powered up by two liquid ZABs with Co/Co_2P@NPSC-3 as the air-cathode (Figure 8g).

Given the high performance of liquid ZABs with Co/Co_2P@NPSC-3, an all-solid ZAB was also fabricated by employing a burnished Zn plate as the anode, Co/Co_2P@NPSC-3 as the cathode catalyst (at the loading of 1.0 mg cm^{-2}) and a solid-state gel as the electrolyte. As depicted in Figure 9a, the OCV was about 1.437 V for Co/Co_2P@NPSC-3. The discharge polarized curve and corresponding power density curve can be shown in Figure 9b, the Co/Co_2P@NPSC-3 ZAB demonstrated a peak power density of 73.9 mW cm^{-2}, which exceeded relevant catalysts reported recently.[63–65] The voltage gap at 25 mA cm^{-2} was about 1.24 V (Figure 9c), implying a stable charge and discharge performance. As depicted in Figure 9d, the round-trip efficiency and voltage gap changed from 56.8% to 46.1% and 0.90 V to 1.23 V for Co/Co_2P@NPSC-3 after the discharge-charge cycling test for 10 h (10 min per cycle). A red LED was lit by three all-solid-state ZABs with Co/Co_2P@NPSC-3 as the air cathode catalysts in series (Figure 9e).

Conclusions

In this work, nanocomposites based on Co/Co_2P nanoparticles encapsulated within hierarchically porous N,P,S co-doped carbon are prepared by ZIF-67and PZS. The resulting Co/Co_2P@NPSC demonstrate apparent catalytic activity towards both ORR and OER, and are used as the reversible oxygen catalyst for ZABs, which exhibited markedly enhanced activity and durability in both liquid and solid electrolytes, as compared to that based on commercial benchmarks of Pt/C and RuO_2. Therefore, this work demonstrates a promising strategy for the synthesis of efficient catalysts based on cobalt phosphide nanoparticles and carbon scaffolds for flexible power sources in wearable electronics applications.

Acknowledgment

L.K thanks the support of the National Natural Science Foundation of China (Nos. 21805170, 22172093, and 21776167), Natural Science Foundation of Shandong Province (Nos. ZR2018BB013), and Youth Innovation Team of Universities in Shandong Province (No. 2019KJC030). Additionally, C.S.W. also thanks the support of the National Science Foundation for this work (CHE-1900235 and CHE-2003685).

Conflict of Interest

The authors declare no conflict of interest.

Keywords: Co/Co_2P nanoparticles · bifunctional electrocatalyst · Zn-air battery · ORR · OER

[1] S. Chu, A. Majumdar, *Nature* **2012**, *488*, 294–303.
[2] T. He, B. Lu, Y. Chen, Y. Wang, Y. Zhang, J. L. Davenport, A. P. Chen, C.-W. Pao, M. Liu, Z. Sun, A. Stram, A. Mordaunt, J. Velasco, Y. Ping, Y. Zhang, S. Chen, *Research* **2019**, *2019*, 6813585.
[3] J.-S. Lee, S. Tai Kim, R. Cao, N.-S. Choi, M. Liu, K. T. Lee, J. Cho, *Adv. Energy Mater.* **2011**, *1*, 34–50.
[4] C. Chakkaravarthy, A. K. A. Waheed, H. V. K. Udupa, *J. Power Sources* **1981**, *6*, 203–228.
[5] T. He, Y. Zhang, Y. Chen, Z. Zhang, H. Wang, Y. Hu, M. Liu, C.-W. Pao, J.-L. Chen, L. Y. Chang, Z. Sun, J. Xiang, Y. Zhang, S. Chen, *J. Mater. Chem. A* **2019**, *7*, 20840–20846.
[6] Z. Ding, Z. Tang, L. Li, K. Wang, W. Wu, X. Chen, X. Wu, S. Chen, *Inorg. Chem. Front.* **2018**, *5*, 2425–2431.
[7] X. Zhu, J. Dai, L. Li, Z. Wu, S. Chen, *Nanoscale* **2019**, *11*, 21302–21310.
[8] P. Peng, L. Shi, F. Huo, S. Zhang, C. Mi, Y. Cheng, Z. Xiang, *ACS Nano* **2019**, *13*, 878–884.
[9] X.-B. Han, X.-Y. Tang, Y. Lin, E. Gracia-Espino, S.-G. Liu, H.-W. Liang, G.-Z. Hu, X.-J. Zhao, H.-G. Liao, Y.-Z. Tan, T. Wagberg, S.-Y. Xie, L.-S. Zheng, *J. Am. Chem. Soc.* **2019**, *141*, 232–239.
[10] Z.-L. Wang, D. Xu, J.-J. Xu, X.-B. Zhang, *Chem. Soc. Rev.* **2014**, *43*, 7746–7786.
[11] Q. Shao, P. Wang, T. Zhu, X. Huang, *Acc. Chem. Res.* **2019**, *52*, 3384–3396.
[12] A. Chen, P. Holt-Hindle, *Chem. Rev.* **2010**, *110*, 3767–3804.
[13] Y.-J. Wang, N. Zhao, B. Fang, H. Li, X. T. Bi, H. Wang, *Chem. Rev.* **2015**, *115*, 3433–3467.
[14] M. Shao, Q. Chang, J.-P. Dodelet, R. Chenitz, *Chem. Rev.* **2016**, *116*, 3594–3657.
[15] W. Xia, A. Mahmood, Z. B. Liang, R. Q. Zou, S. J. Guo, *Angew. Chem. Int. Ed. Engl.* **2016**, *55*, 2650–2676.
[16] T. Zhang, Z. Li, L. Wang, P. Sun, Z. Zhang, S. Wang, *ChemSusChem* **2018**, *11*, 2730–2736.
[17] X. Gao, X. Li, Q. Wang, C. You, X. Tian, C. Wang, Y. Hua, S. Liao, *J. Mater. Chem. A* **2020**, *8*, 2439–2445.
[18] C. Zhu, H. Li, S. Fu, D. Du, Y. Lin, *Chem. Soc. Rev.* **2016**, *45*, 517–531.
[19] H. Wang, W. Wang, Y. Y. Xu, M. Asif, H. Liu, B. Y. Xia, *J. Mater. Chem. A* **2017**, *5*, 17563–17569.
[20] S. Yang, Y. Zhu, C. Cao, L. Peng, W. L. Queen, W. Song, *ACS Appl. Mater. Interfaces* **2018**, *10*, 19664–19672.
[21] J. Li, S. Mao, Y. Hou, L. Lei, C. Yuan, *ChemSusChem* **2018**, *11*, 3292–3298.
[22] S. Zeng, F. Lyu, H. Nie, Y. Zhan, H. Bian, Y. Tian, Z. Li, A. Wang, J. Lu, Y. Y. Li, *J. Mater. Chem. A* **2017**, *7*, 13189–13195.

[23] R. Q. Tianle Gong, Xundao Liu, Hong Li, Yongming Zhang, *Nano-Micro Lett.* **2019**, *11*, 2765–2776.
[24] Y.-N. Zhu, C.-Y. Cao, W.-J. Jiang, S.-L. Yang, J.-S. Hu, W.-G. Song, L.-J. Wan, *J. Mater. Chem. A* **2016**, *4*, 18470–18477.
[25] X. Liu, F. Liu, J. Yu, G. Xiong, L. Zhao, Y. Sang, S. Zuo, J. Zhang, H. Liu, W. Zhou, *Adv. Sci.* **2020**, *7*, 2001526–2001534.
[26] Z. Dai, H. Geng, J. Wang, Y. Luo, B. Li, Y. Zong, J. Yang, Y. Guo, Y. Zheng, X. Wang, Q. Yan, *ACS Nano* **2017**, *11*, 11031–11040.
[27] Z. Fang, L. Peng, Y. Qian, X. Zhang, Y. Xie, J. J. Cha, G. Yu, *J. Am. Chem. Soc.* **2018**, *140*, 5241–5247.
[28] G. Li, J. Yu, J. Jia, L. Yang, L. Zhao, W. Zhou, H. Liu, *Adv. Funct. Mater.* **2018**, *28*, 1801332–1801342.
[29] Y. Yuanyuan, L. Xiongyi, L. Feng, L. Shuwen, L. Xinzhe, N. Siu-Pang, W. C. M. Lawrence, L. Rong, *ChemSusChem* **2018**, *11*, 376–388.
[30] S. Subramani, S. Sathyanarayanan, S. Arumugam, S. Sangaraju, K. S. Ramakrishnan, *Adv. Energy Mater.* **2018**, *8*, 1800555–1800572.
[31] Y. Pan, K. Sun, S. Liu, X. Cao, K. Wu, W.-C. Cheong, Z. Chen, Y. Wang, Y. Li, Y. Liu, D. Wang, Q. Peng, C. Chen, Y. Li, *J. Am. Chem. Soc.* **2018**, *140*, 2610–2618.
[32] M. Zhuang, X. Ou, Y. Dou, L. Zhang, Q. Zhang, R. Wu, Y. Ding, M. Shao, Z. Luo, *Nano Lett.* **2016**, *16*, 4691–4698.
[33] J. Gao, J. Wang, L. Zhou, X. Cai, D. Zhan, M. Hou, L. Lai, *ACS Appl. Mater. Interfaces* **2019**, *11*, 10364–10372.
[34] J. Wang, R. Gao, L. Zheng, Z. Chen, Z. Wu, L. Sun, Z. Hu, X. Liu, *ACS Catal.* **2018**, *8*, 8953–8960.
[35] R. Jin, X. Li, Y. Sun, H. Shan, L. Fan, D. Li, X. Sun, *ACS Appl. Mater. Interfaces* **2018**, *10*, 14641–14648.
[36] L. Yan, L. Cao, P. Dai, X. Gu, D. Liu, L. Li, Y. Wang, X. Zhao, *Adv. Funct. Mater.* **2017**, *27*, 1703455.
[37] Y. Shi, B. Zhang, *Chem. Soc. Rev.* **2016**, *45*, 1529–1541.
[38] X. Tian, X. F. Lu, B. Y. Xia, X. W. Lou, *Joule* **2020**, *4*, 45–68.
[39] S. Yang, L. Peng, P. Huang, X. Wang, Y. Sun, C. Cao, W. Song, *Angew. Chem. Int. Ed. Engl.* **2016**, *55*, 4016–4020.
[40] J.-X. Feng, S.-Y. Tong, Y.-X. Tong, G.-R. Li, *J. Am. Chem. Soc.* **2018**, *140*, 5118–5126.
[41] S. H. Lee, J. Kim, D. Y. Chung, J. M. Yoo, H. S. Lee, M. J. Kim, B. S. Mun, S. G. Kwon, Y.-E. Sung, T. Hyeon, *J. Am. Chem. Soc.* **2019**, *141* 2035–2045.
[42] K. Yuan, D. F. Lützenkirchen-Hecht, L. Li, L. Shuai, Y. Li, R. Cao, M. Qiu, X. Zhuang, Y. Chen, M. K. H. Leung, U. Scherf, *J. Am. Chem. Soc.* **2020**, *142*, 2404–2412.
[43] J. Zhang, Y. Song, M. Kopeć, J. Lee, Z. Wang, S. Liu, J. Yan, R. Yuan, T. Kowalewski, M. R. Bockstaller, K. Matyjaszewski, *J. Am. Chem. Soc.* **2017**, *139*, 12931–12934.
[44] S. Chen, S. Chen, B. Zhang, J. Zhang, *ACS Appl. Mater. Interfaces* **2019**, *11*, 16720–16728.
[45] D. Li, Z. Zong, Z. Tang, Z. Liu, S. Chen, Y. Tian, X. Wang, *ACS Sustainable Chem. Eng.* **2018**, *6*, 5105–5114.
[46] B. Lu, L. Guo, F. Wu, Y. Peng, J. E. Lu, T. J. Smart, N. Wang, Y. Z. Finfrock, D. Morris, P. Zhang, N. Li, P. Gao, Y. Ping, S. Chen, *Nat. Commun.* **2019**, *10*, 631–641.
[47] D. Zhao, X. Zhu, N. Wang, B. Lu, L. Li, S. Chen, *Mater. Today Chem.* **2019**, *11*, 253–268.
[48] Q. Zhang, X. L. Li, B. X. Tao, X. H. Wang, Y. H. Deng, X. Y. Gu, L. J. Li, W. Xiao, N. B. Li, H. Q. Luo, *Appl. Catal. B* **2019**, *254*, 634–646.
[49] Y. Guo, P. Yuan, J. Zhang, H. Xia, F. Cheng, M. Zhou, J. Li, Y. Qiao, S. Mu, Q. Xu, *Adv. Funct. Mater.* **2018**, *28*, 1805641–1805650.
[50] Y. Mun, S. Lee, K. Kim, S. Kim, S. Lee, J. W. Han, J. Lee, *J. Am. Chem. Soc.* **2019**, *141*, 6254–6262.
[51] Y. Ma, S. Luo, M. Tian, J. E. Lu, Y. Peng, C. Desmond, Q. Liu, Q. Li, Y. Min, Q. Xu, S. Chen, *J. Power Sources* **2020**, *450*, 227659–227667.
[52] X. Qiu, X. Yan, H. Pang, J. Wang, D. Sun, S. Wei, L. Xu, Y. Tang, *Adv. Sci.* **2019**, *6*, 1801103–1801111.
[53] T. X. Zhou, W. Zhang, N. Du, Z. Zhong, C. Yan, W. Ju, H. Chu, W. Jiang, H. Wu, C. Xie, Yi., *Adv. Mater.* **2019**, *31*, 1807468–1807476.
[54] X. Wang, H. Xiao, A. Li, Z. Li, S. Liu, Q. Zhang, Y. Gong, L. Zheng, Y. Zhu, C. Chen, D. Wang, Q. Peng, L. Gu, X. Han, J. Li, Y. Li, *J. Am. Chem. Soc.* **2018**, *140*, 15336–15341.
[55] R. Zhang, C. Zhang, W. Chen, *J. Mater. Chem. A* **2016**, *4*, 18723–18729.
[56] H. Jiang, J. Gu, X. Zheng, M. Liu, X. Qiu, L. Wang, W. Li, Z. Chen, X. Ji, J. Li, *Energy Environ. Sci.* **2019**, *12*, 322–333.
[57] Y. P. Zhu, C. Guo, Y. Zheng, S.-Z. Qiao, *Acc. Chem. Res.* **2017**, *50*, 915–923.
[58] Y. Peng, S. Chen, *Green Energy and Environ.* **2018**, *3*, 335–351.
[59] T. Liu, J. Mou, Z. Wu, C. Lv, J. Huang, M. Liu, *Adv. Funct. Mater.* **2020**, *30*, 2003407–2003415.
[60] X. K. Wan, H. B. Wu, B. Y. Guan, D. Luan, X. W. D. Lou, *Adv. Mater.* **2019**, *32*, 1901349–1901356.
[61] K. Song, Z. Zou, D. Wang, B. Tan, J. Wang, J. Chen, T. Li, *J. Phys. Chem. C* **2016**, *120*, 2187–2197.
[62] S. Zhang, L. Wang, L. Fang, Y. Tian, Y. Tang, X. Niu, Y. Hao, Z. Li, *J. Electrochem. Soc.* **2020**, *167*, 054508–054514.
[63] Z. Qian, Y. Chen, Z. Tang, Z. Liu, X. Wang, Y. Tian, W. Gao, *Nano-Micro Lett.* **2019**, *11*, 1–17.
[64] Q. Xu, H. Jiang, Y. Li, D. Liang, Y. Hu, C. Li, *Appl. Catal. B* **2019**, *256*, 117893.
[65] X. Cai, L. Lai, L. Zhou, Z. X. Shen, *ACS Appl. Energ. Mater.* **2019**, *2*, 1505–1516.

Manuscript received: September 14, 2021
Revised manuscript received: October 15, 2021
Accepted manuscript online: October 22, 2021